The Astrophysical Journal, 614:807–817, 2004 October 20

PHOTOEVAPORATED DISKS AROUND MASSIVE YOUNG STARS

Jorge Lugo,[1,2] Susana Lizano,[1] and Guido Garay[3]
Received 2004 March 15; accepted 2004 July 6

ABSTRACT

We present a parametric model of an isothermal photoevaporating wind from a Keplerian disk around a young massive star. The wind is produced by high-energy photons ($h\nu > 13.6$ eV) from the massive central star that ionize and heat the material of the circumstellar disk, as discussed several years ago by Hollenbach and coworkers. The model gives the velocity and density structure of the ionized winds. Because of its simplicity, it is very useful to explore the physical conditions of this type of wind. The model can also describe the photoevaporation of disks around low-mass young stars. We obtain the free-free continuum emission of the photoevaporated flows and compare with the spectral energy distribution of the known bipolar sources MWC 349 A and NGC 7538 IRS 1.

Subject headings: H II regions — hydrodynamics — stars: formation — stars: winds, outflows

1. INTRODUCTION

The photoevaporation of circumstellar disks around massive stars occurs when the disk is ionized and heated by the Lyman continuum photons from the star. A relevant parameter for the dynamical behavior of these winds is the gravitational radius, $r_g \equiv GM_*/a^2 \sim 10^{15} M_{10}$ cm, where G is the gravitational constant, M_* is the mass of the central star, a is the sound speed of the ionized gas ($\sim$10 km s^{-1}), and $M_{10} = M_*/10\,M_\odot$. Within this radius, $r \lesssim r_g$, the heated gas is confined in the gravitational potential well of the star, producing a static ionized dense atmosphere with a temperature $T \sim 10^4$ K. For $r > r_g$, the ionized gas can escape and an isothermal evaporative flow is established. Hollenbach et al. (1994, hereafter H94) studied semianalytically the photoevaporation of these disks. They calculated the transfer of ionizing photons and determined the mass-loss rates of the photoevaporated winds. H94 found that the Lyman continuum flux from the star maintains the ionization of the upper atmosphere but is efficiently attenuated toward the disk; instead, it is the diffuse ionizing radiation produced by recombinations to the ground state that maintains the ionization at the base of the disk. The static atmosphere will exist if the wind of the star is weak. If the star has a strong stellar wind, the wind sweeps away the static dense atmosphere up to a critical radius, $r_w = 10^{16} \dot{M}^2_{w-6} v^2_{w8} \phi^{-1}_{49}$ cm, where the ram pressure of the stellar wind equals the thermal pressure of the photoevaporated flow. In the latter expression $\dot{M}_{w-6}$ is the stellar mass-loss rate in units of $10^{-6}\,M_\odot$ yr^{-1}, v_{w8} is the wind speed in units of 10^8 cm s^{-1}, and ϕ_{49} is the rate of ionizing photons in units of 10^{49} s^{-1}. Yorke & Welz (1996) and Richling & Yorke (1997) carried out hydrodynamical simulations of the evolution of photoevaporated disks under a variety of conditions. In particular, Richling & Yorke (1997) found that scattering of ionizing photons on dust grains increases the photoevaporation rate.

To explain the problem of the large number of ultracompact (UC) H II regions in our Galaxy (Wood & Churchwell 1989) and their short dynamical ages, $\sim 5 \times 10^3$ yr, H94 proposed that UC H II regions, particularly those unresolved or with core/halo morphologies, correspond to photoevaporating disks. The ionized material flows away but is constantly replenished by the photoevaporation of the disk, lengthening the ultracompact phase of UC H II regions to $\sim 10^5$ yr. Recently, Shu et al. (2002) found self-similar models of "champagne flows," namely, ionized regions formed in clouds with steep density gradients where a shock accelerates the gas to supersonic speeds ($v \sim 3a$). They showed that their emission measure (EM) rapidly declines with time below the range of classification as UC H II regions (10^6 cm^{-6} pc $\lesssim$ EM $\lesssim 10^8$ cm^{-6} pc). They noted that UC H II regions with high emission measures are unlikely to correspond to champagne flows, unless mass injection by photoevaporating disks around the central massive star could maintain the EM within the high observed values.

The process of photoevaporation occurs also in disks around low-mass stars. Proplyds in Orion have been explained as disks around low-mass stars that are evaporated by the ionizing radiation from the nearby Trapezium stars, the main exciting source being the most massive star, θ^1 Ori C (e.g., Henney et al. 1996; Johnstone et al. 1998; Störzer & Hollenbach 1999). Johnstone et al. (1998) showed that photoevaporative flows are dominated by either extreme-ultraviolet (EUV) photons ($h\nu > 13.6$ eV) or far-ultraviolet (FUV) photons (6 eV $< h\nu <$ 13.6 eV) depending on the distance to the source of ionizing photons. In EUV-dominated flows, the Lyman continuum photons reach the disk surface and determine the mass-loss rate. In FUV-dominated flows, the longer wavelength photons reach the disk surface and form a photodissociated region (PDR), which consists of a supersonic neutral flow with $v \sim 2$–6 km s^{-1} leaving the disk, a shock, and a thick layer of neutral gas that ends at the ionization front. Thus, the ionization front is detached from the disk as observed in several proplyds. García-Arredondo et al. (2002) have studied the mass loading of the stellar wind of θ^1 Ori C by the photoevaporation of proplyds. Finally, it is interesting to note that the low rate of ionizing photons from low-mass young stars themselves (10^{40}–10^{41} s^{-1}) provides an effective dispersal mechanism in protoplanetary disks for radii greater than $r_g \sim 10$ AU (Shu et al. 1993). These photoevaporative flows have been invoked to explain the low-velocity components observed in the forbidden line spectra of low-mass T Tauri stars (Font et al. 2004).

[1] Centro de Radioastronomía y Astrofísica, Universidad Nacional Autonoma de México, Apartado Postal 72-3 (Xangari), 58089 Morelia, Michoacán, Mexico; s.lizano@astrosmo.unam.mx.
[2] Instituto de Física y Matemáticas, UMSNH, Ciudad Universitaria, C-3, 58040 Morelia, Michoacán, Mexico; j.lugo@astrosmo.unam.mx.
[3] Departamento de Astronomía, Universidad de Chile, Casilla 36-D, Santiago, Chile; guido@das.uchile.cl.

In this work we model the density and velocity structure of axisymmetric isothermal winds photoevaporated from a spatially thin Keplerian disk. In §§ 2–4 we discuss the models in the context of the photoevaporation of disks around massive stars. Nevertheless, it is important to mention that our models can also be applied to the photoevaporation of disks around low-mass stars. In § 5 we compute the free-free continuum emission predicted by these models to compare with the spectral energy distribution (SED) of two well-known massive sources suspected of harboring a photoevaporated disk and obtain physical characteristics of these winds. In § 6 we summarize our results.

2. DISK WIND EQUATIONS

We assume a thin axisymmetric disk at $z = 0$. In steady state, in cylindrical coordinates (ϖ, ϕ, z), the photoevaporated disk wind is governed by the continuity equation

$$\frac{\partial}{\partial \varpi}(\rho v_\varpi) + \frac{\partial}{\partial z}(\rho v_z) = -\frac{\rho v_\varpi}{\varpi} \tag{1}$$

and the three components of the momentum equation

$$v_\varpi \frac{\partial v_\varpi}{\partial \varpi} + v_z \frac{\partial v_\varpi}{\partial z} - \frac{v_\phi^2}{\varpi} = -\frac{1}{\rho}\frac{\partial P}{\partial \varpi} - \frac{\partial \Phi}{\partial \varpi}, \tag{2}$$

$$v_\varpi \frac{\partial v_\phi}{\partial \varpi} + v_z \frac{\partial v_\phi}{\partial z} + \frac{v_\varpi v_\phi}{\varpi} = 0, \tag{3}$$

and

$$v_\varpi \frac{\partial v_z}{\partial \varpi} + v_z \frac{\partial v_z}{\partial z} = -\frac{1}{\rho}\frac{\partial P}{\partial z} - \frac{\partial \Phi}{\partial z}, \tag{4}$$

where ρ is the mass density and v_ϖ, v_ϕ, and v_z are the velocity components in the $\hat{\varpi}$-, $\hat{\phi}$-, and $\hat{z}$-directions, respectively. We assume that the ionizing photons from the star will evaporate material from the disk and heat it to $T \sim 10^4$ K. Thus, the isothermal pressure is

$$P = a^2 \rho, \tag{5}$$

where $a^2 = kT/\mu m_{\rm H}$, k is the Boltzmann constant, μ is the mean molecular weight, and $m_{\rm H}$ is the proton mass. We ignore the disk self-gravity and consider only the stellar gravitational potential given by

$$\Phi = -\frac{GM_*}{\sqrt{\varpi^2 + z^2}}. \tag{6}$$

We follow Blandford & Payne (1982) and choose the nondimensional height ζ and streamline shape function $\chi(\varpi_0, \zeta)$ such that the cylindrical coordinates are

$$\varpi = \chi(\varpi_0,\ \zeta)\varpi_0, \quad \phi = \phi, \quad z = \zeta\varpi_0, \tag{7}$$

where ϖ_0 is the streamline radius at the disk surface, i.e., $\chi(\varpi_0,\ 0) = 1$. We write the normalized velocity components as

$$\frac{v_\varpi}{a} = F(\varpi_0,\ \zeta)\chi'(\varpi_0,\ \zeta), \tag{8}$$

$$\frac{v_\phi}{a} = g(\varpi_0)\mathcal{G}(\varpi_0,\ \zeta), \tag{9}$$

$$\frac{v_z}{a} = F(\varpi_0,\ \zeta), \tag{10}$$

where $\chi' = \partial\chi/\partial\zeta$. We assume that the $\hat{z}$ velocity of injection of the photoevaporated wind at the disk surface has the constant value, i.e., $F(\varpi_0,\ 0) = f_0$. We take $\mathcal{G}(\varpi_0,\ 0) = 1$ and assume that the material at the disk surface is in centrifugal balance with the stellar gravity, i.e., $g(\varpi_0) = \epsilon_0^{1/2}$, where $\epsilon_0 \equiv r_g/\varpi_0$. Finally, we define the density as

$$\rho = \mu m_{\rm H} n(\varpi_0) N(\varpi_0,\ \zeta), \tag{11}$$

where $N(\varpi_0,\ 0) = 1$, $n(\varpi_0)$ is the number density of electron-proton pairs injected at the disk surface, and the mean molecular weight is $\mu = 1.3$.

The differential transformations in terms of the new variables (ϖ_0, ζ) are given by

$$\frac{\partial}{\partial \varpi} = \frac{1}{b_0}\frac{\partial}{\partial \varpi_0} - \frac{\zeta}{b_0 \varpi_0}\frac{\partial}{\partial \zeta},$$
$$\frac{\partial}{\partial z} = -\frac{\chi'}{b_0}\frac{\partial}{\partial \varpi_0} + \frac{1}{b_0}\left(1 + \frac{\partial \ln \chi}{\partial \ln \varpi_0}\right)\frac{\chi}{\varpi_0}\frac{\partial}{\partial \zeta}, \tag{12}$$

with $b_0 \equiv \chi(1 + \partial \ln \chi/\partial \ln \varpi_0) - \zeta\chi'$.

In terms of the new functions, the continuity equation can be integrated as

$$b_0 \chi N F = f_0, \tag{13}$$

and the equation for the azimuthal velocity can also be integrated as

$$\mathcal{G}\chi = 1. \tag{14}$$

The latter expression states that the angular momentum in the $\hat{z}$-direction, $L_z = \varpi v_\phi = (GM_*\varpi_0)^{1/2}$, is conserved.

Finally, the equations for the $\hat{\varpi}$ and $\hat{z}$ velocity components become, respectively,

$$Fb_0 \frac{\partial \chi' F}{\partial \zeta} = -\frac{\partial \ln n}{\partial \ln \varpi_0} - \frac{\partial \ln N}{\partial \ln \varpi_0} + \frac{\partial \ln N}{\partial \ln \zeta} + \frac{\epsilon_0 b_0}{\chi^3} - \frac{\epsilon_0 \chi b_0}{(\chi^2 + \zeta^2)^{3/2}} \tag{15}$$

and

$$Fb_0 \frac{\partial F}{\partial \zeta} = \chi' \frac{\partial \ln n}{\partial \ln \varpi_0} + \chi' \frac{\partial \ln N}{\partial \ln \varpi_0} - \chi\left(1 + \frac{\partial \ln \chi}{\partial \ln \varpi_0}\right)\frac{\partial \ln N}{\partial \zeta} - \frac{\epsilon_0 \zeta b_0}{(\chi^2 + \zeta^2)^{3/2}}, \tag{16}$$

where equation (14) was used.

The solution of equations (15), (16), and (13) gives an exact solution of the wind problem in terms of the new variables (ϖ_0, ζ). In order to obtain a simpler set of equations, we make some further assumptions.

H94 solved the transport of ionizing photons in the photoevaporating wind and found the disk mass-loss rate, which is determined by the flux of ionizing photons that reach the disk surface. Assuming a D-critical ionization front, i.e., $v_z = a$, they found a power-law dependence for the density at the disk surface, $n(\varpi_0) \propto \varpi_0^{-\alpha}$ with $2 < \alpha < 2.5$, the low value of α corresponding to the weak wind case and the high value to the strong wind case. Assuming this power-law behavior of the electron-ion pair number density at the disk surface implies in the

TABLE 1
PARAMETERS OF DISK WIND MODELS

Model	r_g (AU)	α	f_0
1.....	151	2.0	0.2
2.....	151	1.5	0.2
3.....	267	2.3	0.05

above equations that the logarithmic derivative, $\partial \ln n/\partial \ln \varpi_0 = -\alpha$, is constant. Furthermore, we ignore the cross terms $\partial \ln \chi/\partial \ln \varpi_0$ and $\partial \ln N/\partial \ln \varpi_0$. With these assumptions, the equations become a simpler set of coupled differential equations with only ζ derivatives, for the functions χ, F, and N. We show a posteriori that our simplified equations are good approximations, i.e., that the neglected cross terms are small in comparison with the terms that have been taken into account.

3. PARAMETRIC EQUATIONS

With the simplifications discussed at the end of the previous section, and substituting equation (13) into equations (15) and (16), one obtains the set of coupled differential equations

$$\left(\frac{F^2b^2-\zeta^2}{b}\right)\chi'' + \left(\frac{F^2b\chi'+\zeta}{F}\right)F' = (\alpha-1)+\frac{b}{\chi}+\epsilon_0 b\left[\frac{1}{\chi^3}-\frac{\chi}{(\chi^2+\zeta^2)^{3/2}}\right], \quad (17)$$

$$\left(\frac{\zeta\chi}{b}\right)\chi'' + \left(\frac{F^2b-\chi}{F}\right)F' = (1-\alpha)\chi' - \epsilon_0 b\left[\frac{\zeta}{(\chi^2+\zeta^2)^{3/2}}\right], \quad (18)$$

where $b = \chi - \zeta\chi'$ and all the derivatives are done with respect to ζ. For each streamline, these equations, together with the subsidiary equation $\partial\chi/\partial\zeta = \chi'$, can be integrated as ordinary differential equations to obtain the nondimensional functions χ, χ', and F. We call these equations parametric because there is a solution for each different value of the parameter $\epsilon_0 = GM_*/a^2\varpi_0$. From now on, we use ϵ_0 instead of ϖ_0 to label the streamlines.

The boundary conditions at $\zeta = 0$ are

$$F(\epsilon_0,\ 0) = f_0, \quad \chi(\epsilon_0,\ 0) = 1, \quad \chi'(\epsilon_0,\ 0) = 0, \quad (19)$$

where $\chi' = 0$ means that the streamline is perpendicular to the disk surface, although other values of $\chi' > 0$ are allowed.

4. SOLUTIONS

In this section we discuss solutions of our model. We focus the discussion on three different sets of model parameters, chosen such that they closely reproduce the observational characteristics of astrophysical objects (see § 5). The values of the model parameters are summarized in Table 1. The second, third, and fourth columns give, respectively, the gravitational radius, r_g, the power-law exponent of the density at the disk surface, α, and the nondimensional $\hat{z}$ velocity at the disk surface, f_0. The Appendix shows that our equations do not allow the gas to be injected at the sound speed ($f_0 = 1$). Thus, we assume that the injection velocity of the particles at the disk surface is subsonic, $f_0 < 1$, i.e., a weak D-type ionization front.

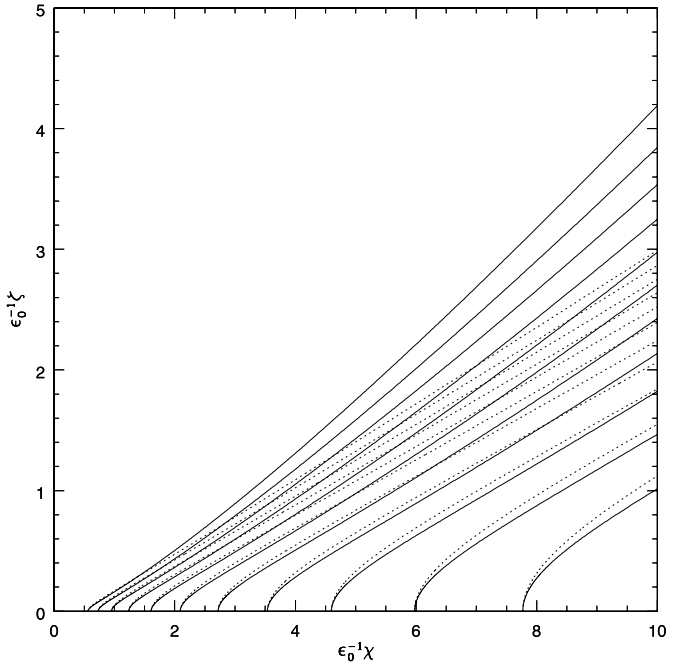

FIG. 1.—Streamlines, $\epsilon_0^{-1}\zeta$ vs. $\epsilon_0^{-1}\chi$. The solid lines correspond to different streamlines of model 1 ($\alpha = 2$), and the dotted lines correspond to different streamlines of model 2 ($\alpha = 1.5$).

Figure 1 shows the nondimensional streamlines, $\epsilon_0^{-1}\zeta$ versus $\epsilon_0^{-1}\chi$. The solid and dotted lines correspond, respectively, to models 1 and 2. Note that these axes translate to the normalized units, $\epsilon_0^{-1}\zeta = z/r_g$ and $\epsilon_0^{-1}\chi = \varpi/r_g$. Figure 1 shows that the streamlines bend with respect to the vertical and become radial very quickly, such that, for $\zeta \gg 1$, the slope of the streamlines, $1/\chi'$, tends to a constant value. This slope is proportional to the injection velocity. In addition, the models with smaller α have smaller streamline slopes than models with larger α.

The top panel of Figure 2 shows in logarithmic scale the nondimensional density, N, as a function of the nondimensional spherical radius, $s \equiv (\zeta^2+\chi^2)^{1/2}$, for different streamlines of model 1 with $0.5 < \epsilon_0 < 2$.

The dotted line has a slope $m = -\alpha = -2$. Along each streamline, the nondimensional density is a power law of the nondimensional spherical radius, $N \rightarrow s^{-\alpha}$. As a consequence, the density defined by equation (11) is a power law of spherical radius, $r = (\varpi^2+z^2)^{1/2}$,

$$\rho = \mu m_{\rm H} n_0 (r/r_g)^{-\alpha}, \quad (20)$$

where n_0 is the density normalization, such that $n(\varpi_0) = n_0\epsilon_0^{\alpha}$. This behavior was already pointed out by Blandford & Payne (1982).

The bottom panel of Figure 2 shows the square of the nondimensional poloidal speed, $(v_p/a)^2 = F^2(\chi'^2+1)$, as a function of the natural logarithm of the nondimensional spherical radius, $\ln s$, for the same streamlines as in the top panel. The dotted line has a slope $m = 2\alpha = 4$. In fact, as in the spherical isothermal wind, Bernoulli's equation implies that, along each streamline, $(v_p/a)^2 \rightarrow 2\alpha \ln(\epsilon_0^{-1}s) = 2\alpha \ln(r/r_g)$, for large spherical radii. A characteristic of these winds is that their speeds are just a few times the sound speed of the ionized gas, a. For distances as large as $r/r_g \sim 150$–1100, i.e., $\ln(\epsilon_0^{-1}s) \sim 5$–$7$, the value of v_p is of the order of $4.5a$.

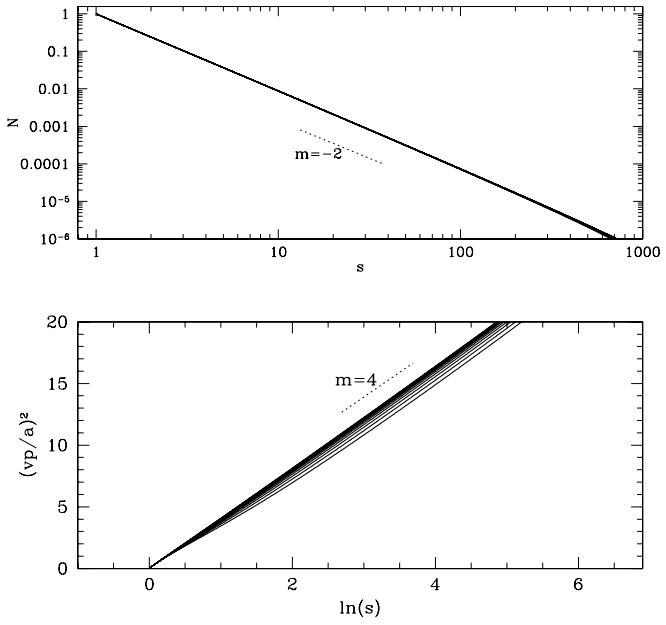

FIG. 2.—*Top*: Nondimensional density, N, vs. nondimensional spherical radius, $s = (\chi^2 + \zeta^2)^{1/2}$, in logarithmic scale, for different streamlines of model 1 with $0.5 < \epsilon_0 < 2$. The dotted line has a slope $m = -\alpha = -2$. *Bottom*: Nondimensional poloidal velocity, v_p/a, vs. natural logarithm of the nondimensional spherical radius, s, for the same streamlines as in the top panel. The dotted line has a slope $m = 2\alpha = 4$.

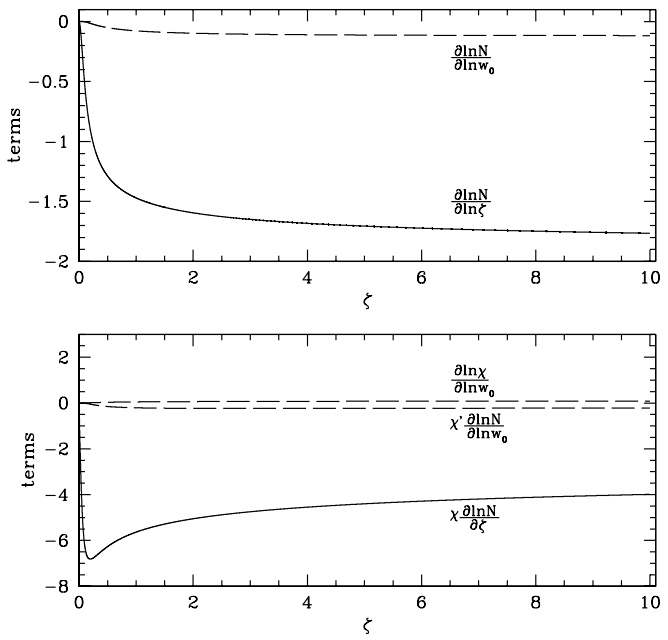

FIG. 3.—*Top*: Values of the terms $\partial \ln N/\partial \ln \varpi_0$ and $\partial \ln N/\partial \ln \zeta$ as a function of ζ, for the streamline with $\epsilon_0 = 2$ in model 1. *Bottom*: Values of the terms $\partial \ln \chi/\partial \ln \varpi_0$, $\chi'(\partial \ln \chi/\partial \ln \varpi_0)$, and $\chi(\partial \ln N/\partial \zeta)$ as a function of ζ, for the same streamline as in the top panel. See discussion in the text.

In order to evaluate the importance of the cross terms that were neglected in our parametric equations (see discussion at the end of § 2), we calculate these terms for different streamlines of model 1. The highest values of the neglected derivatives, $\partial \ln \chi/\partial \ln \varpi_0$ and $\partial \ln N/\partial \ln \varpi_0$, occur for the innermost streamlines. As ϵ_0 decreases, the functions χ and F rapidly tend to the solution with $\epsilon = 0$; thus, these cross terms rapidly go to zero. For model 1 and a streamline with $\epsilon_0 = 2$, the top panel of Figure 3 shows that the magnitude of the cross term $\partial \ln N/\partial \ln \varpi_0$ is small, not only with respect to $\partial \ln n/\partial \ln \varpi_0 = \alpha$, but also with respect to the derivative $\partial \ln N/\partial \ln \zeta$. These terms appear in equation (15). The bottom panel of Figure 3 shows that the magnitude of the cross term $\partial \ln \chi/\partial \ln \varpi_0$ is small compared to 1. It also shows that the magnitude of the cross term $\chi'(\partial \ln N/\partial \ln \varpi_0)$ is small with respect to that of the derivative $\chi(\partial \ln N/\partial \zeta)$. These terms appear in equation (16). Thus, our simplified model indeed takes into account the dominant terms of the equations. We find that depending on the parameters of the models (α, f_0), our equations are valid up to $\epsilon_0 \sim 2$–3, when the magnitude of the derivative, $\partial \ln N/\partial \ln \varpi_0$, becomes $\sim 0.1\alpha$, which we arbitrarily set as a maximum tolerable value. A relaxation method might be used to introduce the neglected cross terms into an exact solution, but this is beyond the scope of this paper.

As discussed above, the limiting factor for solutions to be valid is the magnitude of the cross terms that were neglected in our simplified equations. Empirically, we find that for each value of α there is a maximum value of f_0 for solutions to exist. This maximum value of f_0 decreases with increasing α such that it goes to zero as α goes to 2.5. Finally, the Appendix shows that in the parametric equations the sonic transition occurs at $\zeta > 0$ and is not a critical point of the equations; i.e., the equations are hyperbolic.

5. COMPARISON WITH OBSERVED SOURCES

In this section we present calculations of the free-free continuum emission expected to arise from the density structure of our disk wind models, in order to compare with spectra of observed sources suspected of harboring a photoevaporating disk. The purpose of this comparison is to assess whether or not the spectra of these sources can be explained in terms of photoevaporated disk winds and to obtain the physical parameters of such winds. For simplicity, we consider only winds from disks perpendicular to the plane of the sky (the symmetry axis on the plane of the sky). This approximation is good enough for the sources we want to compare to. Since we assume an isothermal wind, the intensity at frequency ν is given by

$$I_\nu = B_\nu(T)(1 - \exp^{-\tau_\nu}), \tag{21}$$

where $B_\nu(T)$ is the Planck function at temperature T (=10^4 K) and τ_ν is the free-free optical depth $\tau_\nu = \int \kappa_{\rm ff}(\nu)\, ds$, where s is the path length along the line of sight. The free-free opacity is given by

$$\kappa_{\rm ff}(\nu) = \frac{4}{3}\left(\frac{2\pi}{3}\right)^{1/2} \frac{e^6}{m_e^{3/2} hc} \frac{n^2}{\sqrt{kT}} \left[\frac{1 - \exp(-h\nu/kT)}{\nu^3}\right] g_{\rm ff}, \tag{22}$$

where e and m_e are, respectively, the charge and mass of the electron, h is the Planck constant, c is the speed of light, and $g_{\rm ff}$ is the Gaunt factor. The flux density at frequency ν is given by the integral over source solid angle, Ω_S,

$$S_\nu = \int_{\Omega_S} I_\nu \, d\Omega. \tag{23}$$

To calculate the model SEDs from radio to optical frequencies, we interpolate the $g_{\rm ff}$ from the tables of Hummer (1988).

As discussed in § 3, the models of the photoevaporated disk winds depend on several parameters. The solutions depend on the slope of the density profile, α, on the value of the normalized z

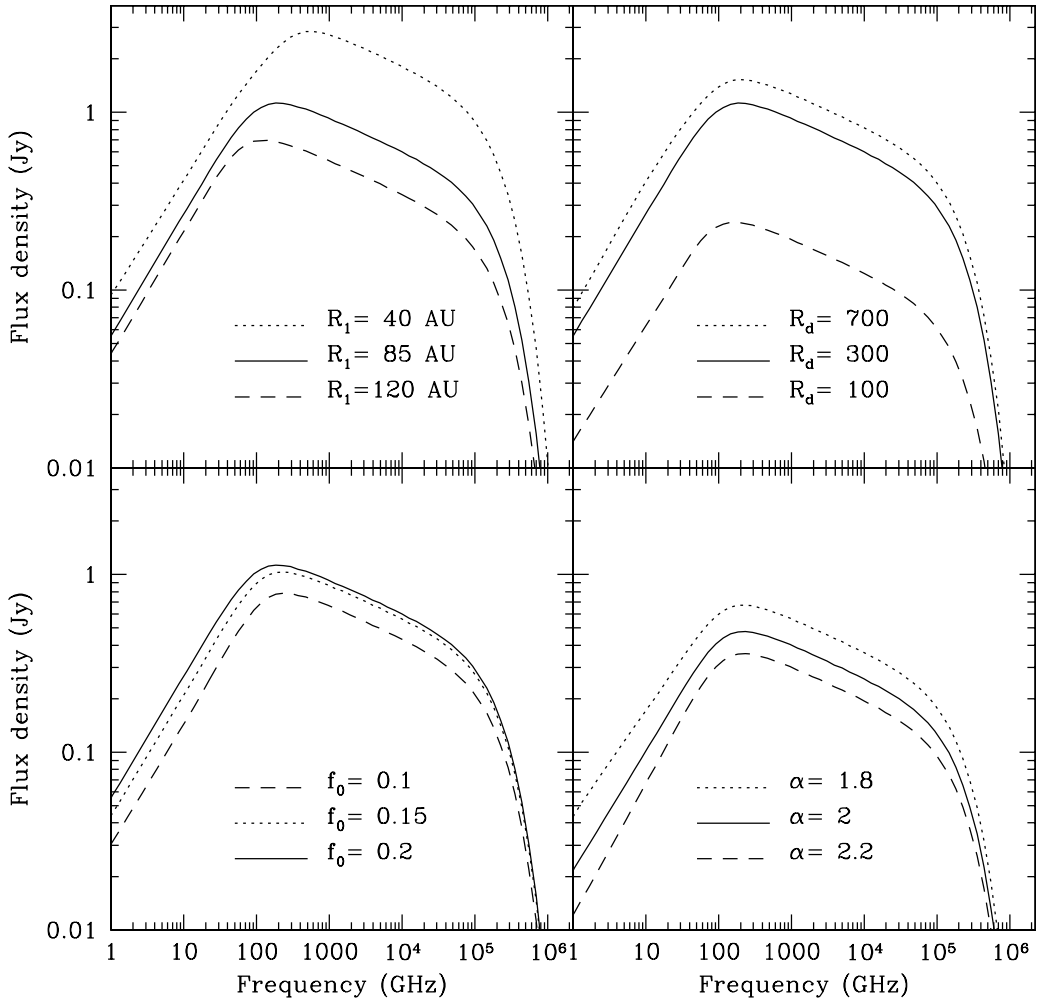

FIG. 4.—Changes in the model spectra due to variations of different model parameters. The reference model (*solid line*) corresponds to model 1 with $R_1 = 85$ AU, $R_d = 300$ AU, and $n_0 = 5 \times 10^6$ cm^{-3}. *Top left*: Effect of changing the inner radius, R_1. *Top right*: Effect of changing the disk radius, R_d. *Bottom left*: Effect of changing f_0. *Bottom right*: Effect of changing α. For the latter set of models we used $f_0 = 0.07$.

velocity at the disk surface, f_0, and on the value of the parameter ϵ_0. For a given gravitational radius, the parameter $\epsilon_0 = r_g/\varpi_0$ labels each streamline. Given the nondimensional density, N, to obtain the density of the wind, one has to specify its value at the disk surface, $n(\epsilon_0) = n_0\epsilon_0^{\alpha}$ (see eq. [11]). Furthermore, to obtain the free-free emission, we need to specify the wind's inner radius, R_1, and the disk radius, R_d, which determine the range in which streamlines are built at the surface of the disk ($R_1 \leq \varpi_0 \leq R_d$). In addition, the photoevaporated wind free-free emission will be proportional to the disk mass-loss rate, $\dot{M}_d$, given by

$$\dot{M}_d = 4\pi \int_{R_1}^{R_d} \rho u \varpi_0 \, d\varpi_0 = \begin{cases} 4\pi\mu m_{\rm H} n_0 f_0 a r_g^2 \dfrac{1}{2-\alpha}\left[\left(\dfrac{R_d}{r_g}\right)^{2-\alpha} - \left(\dfrac{R_1}{r_g}\right)^{2-\alpha}\right], & \alpha \neq 2, \\ 4\pi\mu m_{\rm H} n_0 f_0 a r_g^2 \ln\left(\dfrac{R_d}{R_1}\right), & \alpha = 2. \end{cases} \quad (24)$$

Now we discuss the effects produced on the free-free spectra by changing different parameters of the models. For this purpose we consider model 1 as a reference model, with $R_1 = 85$ AU, $R_d = 300$ AU, and $n_0 = 5 \times 10^6$ cm^{-3}. To calculate the model free-free spectrum, we assume that the source is at a distance of 1.2 kpc. We consider the effect of varying one parameter at a time. The top left panel of Figure 4 shows the changes in the spectra due to changes in the inner radius. As R_1 decreases, the emission increases and the frequency of turnover to the optically thin regime becomes higher. This happens because the most inner streamlines have the highest density since $n(\epsilon_0) \propto \epsilon_0^{\alpha}$. The top right panel of Figure 4 shows the effect of changing the disk radius, R_d. The emission increases as R_d increases, although there is not much flux coming from streamlines beyond 700 AU. The bottom left panel of Figure 4 shows that increasing f_0 increases the emission because the density increases (see eq. [13]). The bottom right panel of Figure 4 shows the effect of changing α. For this set of models we used $f_0 = 0.07$ because this is the maximum value allowed for models with $\alpha = 2.2$. The change of the slope of the emission at radio wavelengths, due to the density dependence $N = s^{-\alpha}$, discussed in § 4 is clearly seen in this panel.

In what follows we discuss the modeling of the SED of two well-known bipolar sources, suspected of harboring a photoevaporated disk: MWC 349 A and NGC 7538 IRS 1.

5.1. *MWC 349 A*

MWC 349 A, the brightest radio source in the sky, is a member of a binary system at a distance of 1.2 kpc. MWC 349 A

is a Be star with a luminosity $L \sim 3 \times 10^4\ L_\odot$ and a rate of ionizing photons $\phi > 10^{48}\ s^{-1}$ (Cohen et al. 1985). MWC 349 B (at a distance of 2.″4, ~2880 AU) is classified as B0 III. An arc of enhanced radio emission shows the interaction between winds from the two stars (Cohen et al. 1985; Tafoya et al. 2004). The continuum spectrum of MWC 349 A exhibits a power-law behavior $S_\nu \propto \nu^{0.6}$ from 90 cm to ~100 μm (e.g., Harvey et al. 1979; Dreher & Welch 1983). The high angular resolution centimeter maps show a bipolar morphology (White & Becker 1985; Cohen et al. 1985; Martín-Pintado et al. 1993; Tafoya et al. 2004). Using infrared speckle interferometry, Leinert (1986) inferred the presence of a hot dusty disk with a size ~100 AU. Using the Keck I telescope, Danchi et al. (2001) obtained spectacular near-IR disklike images with $R \sim 44$–75 AU. Unfortunately, the astrometry of the latter work is not adequate to securely put this disk emission at the center of the source. Hamann & Simon (1986) found near-IR double-peaked emission lines they interpreted as arising from both the ionized flow and neutral material from a rotating disk. Radio recombination lines indicate a terminal velocity in the ionized flow of $v \sim 25$–50 km s^{-1}, whereas radio continuum observations indicate a mass-loss rate of $\dot{M}_w \sim 10^{-5}\ M_\odot$ yr (e.g., Altenhoff et al. 1981; Hartmann et al. 1980; Dreher & Welch 1983). Masing hydrogen radio recombination lines (RRLs) at centimeter and millimeter wavelengths have been interpreted as coming from a disk radius ~30 AU with $n \sim 10^7$ cm^{-3} (e.g., Martín-Pintado et al. 1989, 1993, 1994; Gordon 1992, 2003; Planesas et al. 1992; Thum et al. 1992). From observations of the H92α RRL emission with angular resolution, Rodríguez & Bastian (1994) proposed that the observed velocity field can be explained by an ionized rotating and expanding envelope. Far-infrared recombination lines also show stimulated emission (e.g., Strelnitski et al. 1996).

Figure 5 shows the SED of MWC 349 A. The data points correspond to observations reported in the literature from 21 cm to U wavelengths (0.36 μm). These data are summarized in Table 2. We model the free-free emission from this source as arising from two components: a photoevaporated disk wind and a hydrostatic atmosphere close to the star, which corresponds to the weak-wind case discussed by H94. The solid line corresponds to the results of the model with the best fit to the spectrum shortward of 300 GHz. The dotted line corresponds to the emission of the photoevaporated disk wind alone, with the parameters of model 1. The value of r_g(=151 AU) corresponds to that of a star with $M_* = 17\ M_\odot$. This star has a main-sequence luminosity $L = 3 \times 10^4\ L_\odot$ according to the stellar structure models of Schaller et al. (1992). The wind's inner radius and the disk radius are 85 and 300 AU, respectively. The wind density at the disk surface is given by $n(\varpi_0) = n_0 \epsilon_0^2$, where $n_0 = 5.0 \times 10^6$ cm^{-3}. The dot-dashed line corresponds to the emission of the hydrostatic atmosphere located between $R_a < r < R_1$, where the atmosphere's inner radius is $R_a = 6.6$ AU. The density of this atmosphere is given by $n(r, z) = n_1 (r/R_1)^{-3/2} \exp(-z^2/2H^2)$, where $n_1 = 3.5 \times 10^6$ cm^{-3} and the scale height is $H = r_g (r/r_g)^{3/2}$ (see H94). The emission of this dense atmosphere is required to maintain the ionized material optically thick up to ~1 mm. The disk mass-loss rate of this model, given by equation (24), is $2.8 \times 10^{-6}\ M_\odot$ yr^{-1}.

As expected, the density power law, $\rho \propto r^{-2}$ (eq. [20]), produces a power-law emission with $S_\nu \propto \nu^{0.6}$ (e.g., Panagia & Felli 1975). Such a decreasing density profile produces envelopes that are partially optically thick, such that the surface of $\tau_\nu \sim 1$ increases with decreasing frequency. The resulting frequency-size dependence for MWC 349 A, $\theta \propto \nu^{-0.7}$, was recently measured by Tafoya et al. (2004), confirming the presence of a wind.

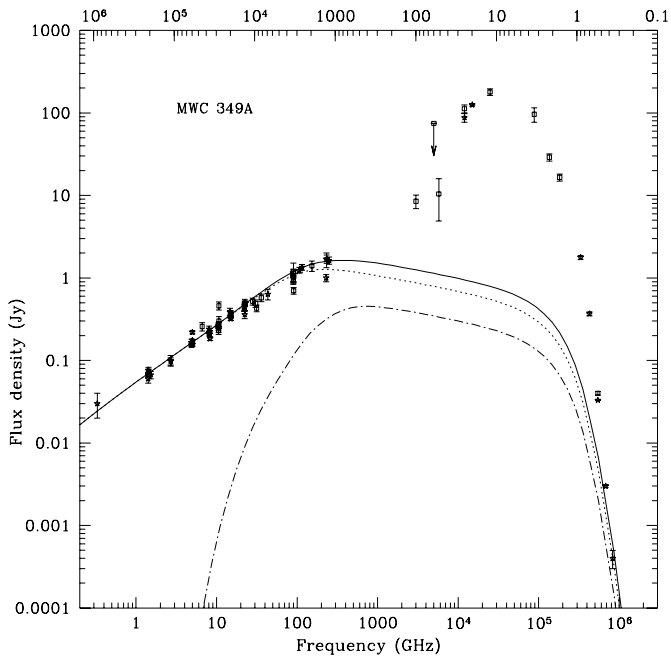

FIG. 5.—SED of MWC 349 A. The upper axis is labeled in μm. The data points are summarized in Table 2. The squares denote data obtained with low angular resolution observations ($\theta_{\rm beam} > 12''$). The solid line corresponds to the free-free emission from a model of a photoevaporated disk wind and a hydrostatic atmosphere that best fitted the spectrum shortward of 300 GHz. The dotted line shows the emission of the photoevaporated disk wind alone (with the parameters of model 1; see Table 1), and the dot-dashed line shows the emission of the hydrostatic atmosphere alone (see parameters in text). We assumed an attenuation $A_V = 2$.

The excess emission (with respect to the free-free emission) observed at far- and mid-infrared wavelengths is most likely due to dust emission. Since MWC 349 is not embedded inside a molecular cloud, the dust emission must come from either the circumstellar disk itself or dust embedded inside the ionized disk wind. We are currently in the process of modeling this far- and mid-infrared dust emission and have found that the most likely source is hot dust within the disk wind itself.

Being at the distance of 1.2 kpc, one expects an interstellar extinction at optical wavelengths, $A_V \sim 2$, toward MWC 349 A (e.g., Vergely et al. 1997). The model spectrum has been attenuated according to the optical and infrared analytic fit to the interstellar extinction law given by Cardelli et al. (1989), with an optical total-to-selective extinction ratio $R = A_V/E(B-V) = 3.2$. Figure 5 shows that an interstellar extinction, $A_V \sim 2$, is barely enough to decrease the model emission within the observational values at B and U bands. Any dust within the photoevaporated wind will also attenuate the free-free emission at these high frequencies. Thus, we leave this problem to the self-consistent calculation that includes dust emission and absorption.

5.2. *NGC 7538 IRS 1*

NGC 7538 consists of a cluster of H II regions in different stages of development located at 2.8 kpc (Blitz et al. 1982). It has three compact dust-embedded H II regions, referred to as NGC 7538 IRS 1, IRS 2, and IRS 3 (Martin 1973; Wynn-Williams et al. 1974). NGC 7538 IRS 1 is a UC H II region with a size less than 2″ and a bipolar morphology (e.g., Campbell

TABLE 2
MWC 349 A Observations

ν (GHz)	S (Jy)	Angular Resolution (arcsec)	References
0.3.....	0.0106 ± 0.0026	5.38 × 5.15	1
1.4.....	0.060 ± 0.007	13–11	2
	0.068 ± 0.003	13–11	3
	0.070 ± 0.007[a]	60 × 90	4
	0.0764 ± 0.0064	1.33 × 1.15	1
1.5.....	0.067 ± 0.007[a]	5	5
2.7.....	0.098 ± 0.010	3	6
	0.100 ± 0.015	3	7
4.9.....	0.1548 ± 0.0085	0.38 × 0.36	1
	0.1659 ± 0.016[a]	0.337 × 0.320	8
5.....	0.155 ± 0.005	0.3	9
	0.155 ± 0.007	3.7	3
	0.175 ± 0.005	3.7	3
	0.220 ± 0.10	3	10
6.6.....	0.257 ± 0.030	260	11
8.1.....	0.208 ± 0.010	1	6
	0.240 ± 0.020	1	7
	0.220 ± 0.010	1–10	12
8.3.....	0.210 ± 0.02	0.3	13
	0.1835 ± 0.0095	0.22 × 0.20	1
10.5.....	0.265 ± 0.020	168	14
	0.253 ± 0.020	168	11
10.6.....	0.230 ± 0.023[a]	160	15
	0.234 ± 0.016	160	16
10.7.....	0.300 ± 0.040	80	17
	0.460 ± 0.050	80	17
	0.270 ± 0.025	75	3
14.7.....	0.390 ± 0.040[a]	4	18
14.9.....	0.3800 ± 0.0212	0.13 × 0.11	1
15.0.....	0.320 ± 0.015	0.15	9
	0.358 ± 0.015	54	19
	0.340 ± 0.034[a]	0.38 × 0.15	20
22.2.....	0.434 ± 0.042	78	16
22.4.....	0.4462 ± 0.0448	0.085 × 0.077	1
	0.360 ± 0.04	0.067 × 0.065	21
22.5.....	0.500 ± 0.05	0.49 × 0.13	20
	0.495 ± 0.030	35	19
28.0.....	0.520 ± 0.050	28	19
30.5.....	0.490 ± 0.05	105	22
31.4.....	0.430 ± 0.040[a]	230	23
36.0.....	0.575 ± 0.060[a]	101	24
43.4.....	0.6350 ± 0.0956	0.038 × 0.034	1
89.6.....	1.020 ± 0.11	80	22
90.0.....	1.056 ± 0.221	80	16
	1.140 ± 0.060	210	25
	1.190 ± 0.330	80	19
91.0.....	0.699 ± 0.065	75	26
	1.020 ± 0.126	75	26
91.1.....	0.960 ± 0.07	25	27
106.8.....	1.24 ± 0.10	3.2 × 2.2	28
115.3.....	1.35 ± 0.11	4 × 9.6	28
152.6.....	1.400 ± 0.20	48	22
230.0.....	1.00 ± 0.10[a]	12.3	29
231.9.....	1.67 ± 0.34	0.70 × 0.84	30
232.4.....	1.70 ± 0.20	11.5	27
250.0.....	1.630 ± 0.163	11.2	31
2997.9.....	8.50 ± 1.60	37	32
4996.5.....	<74.6	60	33
5765.2.....	10.4 ± 5.5	37	32
11991.7.....	87.50 ± 10.41	13	34
	112.4 ± 12.36[b]	60	33
14989.6.....	125.33 ± 4	13	34
24982.7.....	179 ± 16.11[b]	60	33
88174.3.....	95.93 ± 19	7–35	35
136269.3.....	28.99 ± 2.89	7–35	35
182800.3.....	16.54 ± 1.65	7–35	35
333102.7.....	1.77 ± 0.09	1	36
428274.9.....	0.368 ± 0.02	1	36
545077.2.....	0.040 ± 0.002	7–35	35
	0.033	1	36
681346.5.....	0.0030	1	36
832756.8.....	0.0004	1	36

[a] Assumed error is 10% of observed flux.
[b] Error taken from Beichman et al. (1988).

References.—(1) Tafoya et al. 2004; (2) Braes et al. 1972; (3) Altenhoff et al. 1976; (4) Wendker et al. 1991; (5) Zoonematkermani et al. 1990; (6) Wink et al. 1982; (7) Hjellming et al. 1973; (8) Cohen et al. 1985; (9) White & Becker 1985; (10) Baldwin et al. 1973; (11) Gregory & Seaquist 1973; (12) Greenstein 1973; (13) Rodríguez & Bastian 1994; (14) Hughes & Woodsworth 1973; (15) Woodsworth & Hughes 1977; (16) Purton et al. 1982; (17) Altenhoff & Wendker 1973; (18) Escalante et al. 1989; (19) Altenhoff et al. 1981; (20) Dreher & Welch 1983; (21) Martín-Pintado et al. 1993; (22) Schwartz 1980; (23) Perrenod & Lada 1979; (24) Nesterov 1990; (25) Ulich 1981; (26) Schwartz & Spencer 1977; (27) Martín-Pintado et al. 1989; (28) Martín-Pintado et al. 1994; (29) Steppe et al. 1988; (30) Planesas et al. 1992; (31) Altenhoff et al. 1994; (32) Harvey et al. 1979; (33) Beichman et al. 1988; (34) Simon & Dyck 1977; (35) Allen 1973; (36) Lee 1970.

1984; Turner & Matthews 1984; Gaume et al. 1995). The exciting source has a luminosity $L > 8 \times 10^4\ L_\odot$, a spectral type earlier than O7.5, and a rate of ionizing photons $\phi > 10^{48}\ \mathrm{s}^{-1}$ (e.g., Hackwell et al. 1982; Akabane et al. 2001). NGC 7538 IRS 1 is surrounded by millimeter and submillimeter dust emission (e.g., Scoville et al. 1986; Woody et al. 1989; Akabane et al. 1992, 2001; Momose et al. 2001) and by dense and warm molecular gas, which has been observed in emission in HCN (Pratap et al. 1989) and in absorption in $NH_3(3, 3)$ lines (Henkel et al. 1984). It is also associated with a high-velocity molecular outflow and an elongated ^{13}CO large-scale flattened structure, orthogonal to the outflow symmetry axis, with a diameter of ~60,000 AU and oriented in the east-west direction (e.g., Campbell & Thompson 1984; Scoville et al. 1986). Several maser species have been detected toward this source (OH, H_2O, H_2CO, CH_3OH, and NH_3) coming from the interface between the ionized and molecular gas (e.g., Downes & Wilson 1974; Dickel et al. 1982; Forster et al. 1982; Norris et al. 1982; Kameya et al. 1990; Rots et al. 1981; Menten et al. 1988; Madden et al. 1986). VLBI observations of methanol masers show a linear structure with a velocity gradient indicative of a Keplerian disk seen edge-on (Minier et al. 1998, 2000). The methanol maser emission has been recently modeled as arising from such a disk by Pestalozzi et al. (2004). High-resolution observations of the H66α RRL show an extremely wide line profile, $\Delta v_{\mathrm{FWZI}} \sim 250\ \mathrm{km\ s^{-1}}$, interpreted as a slow stellar wind with a velocity $v \sim 300\ \mathrm{km\ s^{-1}}$ (Gaume et al. 1995). Recently, Franco-Hernández & Rodríguez (2004) found a decrease in the centimeter emission of the lobes (of order 20%–30%) over an interval of 11 yr, which they interpret as being due to an increase in the absorption of ionizing photons in the core region. In this respect, it is interesting to note that Hollenbach has suggested that inhomogeneities (clumps) in the photoevaporation process could produce time variability observed in RRLs (quoted in Gordon 2003).

Figure 6 shows the SED of NGC 7538 IRS 1. The data points are observations reported in the literature from 18 cm to U wavelengths (0.36 μm). These data are summarized in

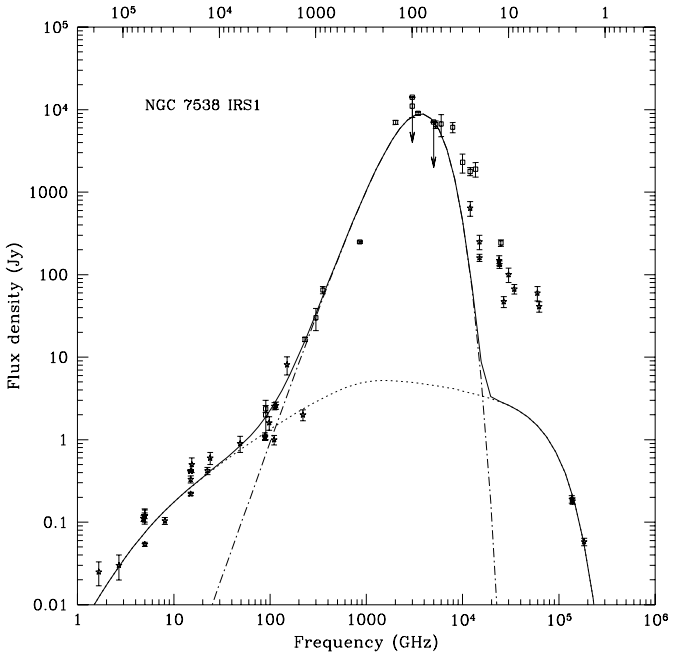

FIG. 6.—SED of NGC 7538 IRS 1. The upper axis is labeled in μm. The data points are summarized in Table 3. The squares denote data obtained with low angular resolution observations ($\theta_{\rm beam} > 12''$). The dotted line corresponds to the emission of the photoevaporated disk wind that best fitted the SED shortward of 200 GHz (with the parameters of model 3; see Table 1). The dot-dashed line shows the emission of a modified blackbody with a temperature $T_d = 46$ K and a solid angle $\Omega_d = \pi(12\farcs5)^2$. We assumed an attenuation $A_V = 17$ (see text).

Table 3. We model the free-free emission from this source as fully arising from a photoevaporated disk wind, which corresponds to the strong-wind case discussed by H94. The dotted line corresponds to the model emission from a disk wind with the parameters of model 3. The value of r_g(=267 AU) corresponds to that of a star with $M_* = 30\ M_\odot$. This star has a main-sequence luminosity $L = 10^5\ L_\odot$ according to the stellar structure models of Schaller et al. (1992). The model has a wind's inner radius of $R_1 = 115$ AU and a disk radius of $R_d = 500$ AU. The inner radius would correspond to the critical radius, r_w, mentioned in § 1, for a slow stellar wind with $v_w \sim 300$ km s^{-1} and $\dot{M}_w \sim 1 \times 10^{-6}\ M_\odot$ yr^{-1}. The wind density at the disk surface is given by $n(\varpi_0) = n_0 \epsilon_0^{2.3}$, where $n_0 = 2.2 \times 10^7$ cm^{-3}. The disk mass-loss rate of this model, given by equation (24), is $1.1 \times 10^{-5}\ M_\odot$ yr^{-1}. For this source the power-law density, $\rho \propto r^{-2.3}$ (eq. [20]), produces a steeper power-law emission, $S_\nu \propto \nu^{0.8}$. In fact, given the dispersion in the observed fluxes, this source can also be fitted with similar models with $2.1 \leq \alpha \leq 2.3$. Since the source is immersed within a dense molecular cloud, the photoevaporated wind was considered to have a finite size $\theta \sim 2\farcs5$. Thus, for $\nu \lesssim 3$ GHz all the wind material is completely optically thick and the spectrum tends to $S_\nu \propto \nu^2$.

As discussed above, NGC 7538 IRS 1 is embedded in a dense molecular cloud. Thus, the model spectrum has been attenuated according to the optical and infrared analytic fit to the interstellar extinction law given by Cardelli et al. (1989), with a visual extinction $A_V = 17$ and an optical total-to-selective extinction ratio $R = A_V/E(B-V) = 3.2$. In addition, one expects dust emission at far- and mid-infrared wavelengths from the surrounding molecular gas. To illustrate this, the dot-dashed line in Figure 6 corresponds to the modified blackbody dust emission, $S_d(\nu) = B_\nu(T_d)(1 - \exp^{-\tau_{d\nu}})\Omega_d$, expected from

TABLE 3
NGC 7538 IRS 1 OBSERVATIONS

ν (GHz)	S (Jy)	Angular Resolution (arcsec)	References
1.7.....	0.025 ± 0.008	1.2	1
2.7.....	0.03 ± 0.01	7.5 × 5.1	2
4.8.....	0.111 ± 0.009	0.49 × 0.41	3
5.0.....	0.120 ± 0.010	0.356	4
	0.120 ± 0.025	3.7	5
	0.054 ± 0.003	0.4	6
	0.120 ± 0.020	2.1 × 2.6	7
8.1.....	0.104 ± 0.010	2.5 × 1.7	2
15.0.....	0.220 ± 0.011	0.13	6
	0.331 ± 0.033[a]	0.14	8
	0.418 ± 0.010	0.36 × 0.34	4
15.4.....	0.500 ± 0.100	0.65	9
22.4.....	0.420 ± 0.042[a]	0.11	10
23.9.....	0.600 ± 0.100	2.5 × 2.2	11
49.0.....	0.900 ± 0.200	6.0 × 5.5	12
88.6.....	1.1 ± 0.11[a]	8.9 × 8.5	13
88.7.....	1.06 ± 0.08	2.9 × 2.6	14
90.0.....	2.0 ± 1.0	45	12
	2.37 ± 0.23[a]	30	15
98.0.....	1.600 ± 0.300	2.9 × 2.3	12
110.2.....	0.996 ± 0.13	4.6 × 3.3	16
111.0.....	2.550 ± 0.255[a]	7	17
115.3.....	2.600 ± 0.26[a]	3.3	18
149.9.....	8.1 ± 2	12	19
219.5.....	2.0 ± 0.3	3	18
230.6.....	16.4 ± 10	90	20
299.8.....	30. ± 9	55	21
352.7.....	65 ± 6.5[a]	14	22
856.5.....	249 ± 7	30	20
2012.0.....	7000 ± 410	50	23
2997.9.....	11000 ± 3000	55	21
	<14140	180	24
3445.9.....	9000 ± 350	50	23
4996.5.....	<7073	90	24
5259.5.....	6600 ± 700	30	23
5995.8.....	6700 ± 2000	40	21
7889.3.....	6100 ± 870	50	23
9993.1.....	2300 ± 600	40	21
11991.7.....	640 ± 130	6	21
	1780 ± 196[b]	44	24
13626.9.....	1900 ± 380	50	23
14989.6.....	160 ± 16[a]	3.5	25
	250 ± 50	5	21
23983.4.....	149 ± 21	7.5	21
24176.8.....	133 ± 14	4	26
24982.0.....	242 ± 22[b]	45	24
26767.2.....	47 ± 7	7.5	21
29979.2.....	100 ± 20	3.5	25
34458.9.....	67 ± 9	7.5	21
59958.5.....	60 ± 12	3.5	25
62456.8.....	41 ± 6	7.5	21
136269.3.....	0.190 ± 0.020	5	21
138921.4.....	0.181 ± 0.016	1	27
182800.3.....	0.058 ± 0.006	1	27

[a] Assumed error is 10% of observed flux.
[b] Error taken from Beichman et al. (1988).

REFERENCES.—(1) Dickel et al. 1982; (2) Akabane et al. 2001; (3) Rots et al. 1981; (4) Campbell 1984; (5) Israel 1977; (6) Franco-Hernandez & Rodríguez; (7) Martin 1973; (8) Turner & Matthews 1984; (9) Harris & Scott 1976; (10) Gaume et al. 1995; (11) Henkel et al. 1984; (12) Akabane et al. 1992; (13) Pratap et al. 1989; (14) Pratap 1990; (15) Steppe et al. 1993; (16) Odenwald et al. 1992; (17) Scoville et al. 1986; (18) Woody et al. 1989; (19) Pratap et al. 1992; (20) Chini & Krugel 1986; (21) Werner et al. 1979; (22) Momose et al. 2001; (23) Thronson & Harper 1979; (24) Beichman et al. 1988; (25) Hackwell et al. 1982; (26) Wink et al. 1975; (27) Bloomer et al. 1998.

dust with a temperature T_d of 46 K and a solid angle $\Omega_d = \pi(12\farcs5)^2$. For the dust opacity we took the rough approximation, $\tau_{d\nu} = 0.025(\nu/300\ \mathrm{GHz})^{1.3}$, valid for millimeter wavelengths. As discussed for the case of MWC 349 A, the emission at near-IR and optical wavelengths could come from dust embedded in the ionized disk wind.

5.3. *Comments and Caveats*

It is worthwhile at this point to discuss some of the assumptions made in our photoevaporated wind model. Given a mass injection at the disk surface, we solve for the wind dynamics. We do not solve for the transport of the ionizing radiation to determine the particle flux at the disk surface (as H94 did, assuming the wind dynamics). This could be done in an iterative fashion: given a particle flux at the disk surface, one can use the corresponding parametric solutions to calculate the transport of the ionizing radiation to determine a new particle flux at the disk surface. The only constraint is that the particle density at the disk surface has to be smoothed to a power law, $n(\epsilon_0) \propto \epsilon_0^{\alpha}$, as required by the parametric equations.

Our disk winds are thermal winds, driven by pressure gradients. We do not take into account acceleration of the gas due to radiation pressure on absorption lines or on dust embedded in the wind, which will be deferred for a future study. Furthermore, we do not follow the disk evolution subject to photoionization and viscous accretion/spreading (e.g., Clarke et al. 2001; Matsuyama et al. 2003) but instead treat the disk as a source of mass. For the typical mass-loss rates expected in photoevaporating disks $\dot{M} \sim 10^{-5}\ M_{\odot}\ \mathrm{yr}^{-1}$, disks around massive stars more massive than 1 $M_{\odot}$ could sustain photoevaporative flows for timescales $\Delta t > 10^5$ yr.

As discussed earlier in this section, one important aspect for comparison with observed SEDs is the contribution of dust embedded in the wind at far- and mid-IR wavelengths. We are currently modeling this dust emission including a total free-free plus dust opacity in the integration of the intensity along the line of sight.

6. SUMMARY

We have presented axisymmetric models of winds photoevaporating from a Keplerian thin disk around a massive star. The model parameters are the gravitational radius, r_g, the power-law exponent of the density at the disk surface, α, and the injection velocity at the disk surface, f_0. The equations are solved for each streamline, defined by the value of the parameter $\epsilon_0 = r_g/\varpi_0$. The models can also describe the photoevaporation of disks around low-mass young stars either immersed in an ionizing photon field of a neighboring massive star or subject to the relatively low rate of ionizing photons of the low-mass star itself.

The solution for each streamline depends on the value of the parameter $\epsilon_0 = r_g/\varpi_0$, where ϖ_0 is the streamline radius at the disk surface. The models are very simple to construct and can be used to compare with observed sources and infer the physical conditions of photoevaporated disk winds. We applied these models to two well-known bipolar UC H II regions.

The SED of MWC 349 A for $\nu < 300$ GHz is very well fitted by a model of a photoevaporated disk wind with a hydrostatic atmosphere close to the central star. The best fit is provided by a model with a gravitational radius of 151 AU and a photoevaporated disk wind with a wind density at the disk surface with a power-law exponent of 2 and a density normalization of $5.0 \times 10^6\ \mathrm{cm}^{-3}$. The disk radius is 300 AU and the wind's inner radius is 85 AU. A dense hydrostatic atmosphere with an inner radius of 6.6 AU is required to maintain the ionized material optically thick up to $\sim$1 mm.

The SED of NGC 7538 IRS 1 for $\nu < 200$ GHz is well fitted by a model of a photoevaporated disk wind, with a gravitational radius of 267 AU, a wind's inner radius of 115 AU, a disk radius of 500 AU, a wind density at the disk surface with a power-law exponent of 2.3, and a density normalization of $2.2 \times 10^7\ \mathrm{cm}^{-3}$.

We find that the process of photoevaporation of disks around massive stars can produce spectral signatures up to frequencies as high as 1 mm. Thus, to distinguish the free-free emission from the photoevaporated material from the dust emission of the circumstellar disk itself, one needs high-resolution observations over a wide range of frequencies, in particular, at $\lambda < 1$ mm. Observations with the recently available Submillimeter Array will help to better understand the nature of this type of source.

We are grateful to an anonymous referee for very helpful suggestions. We thank Paola D'Alessio, Yolanda Gómez, and Luis Rodríguez for useful discussions. J. L. and S. L. acknowledge support from DGAPA/UNAM IN104202 and CONACyT 40091. G. G. acknowledges support from the Chilean Centro de Astrofísica FONDAP 15010003 and FONDECYT project 1010531.

APPENDIX

CRITICAL POINTS OF THE PARAMETRIC EQUATIONS

The parametric equations (17) and (18) can be written in the synthetic form

$$a_1\chi'' + b_1F' = c_1 \tag{A1}$$

and

$$a_2\chi'' + b_2F' = c_2, \tag{A2}$$

where

$$a_1 = \frac{F^2b^2 - \zeta^2}{b}, \qquad b_1 = \frac{F^2b\chi' + \zeta}{F}, \qquad c_1 = (\alpha - 1) + \frac{b}{\chi} + \epsilon_0 bd_1,$$
$$a_2 = \frac{\zeta\chi}{b}, \qquad b_2 = \frac{F^2b - \chi}{F}, \qquad c_2 = (1 - \alpha)\chi' - \epsilon_0 bd_2, \tag{A3}$$

given

$$d_1 = \left[\frac{1}{\chi^3} - \frac{\chi}{(\chi^2+\zeta^2)^{3/2}}\right], \qquad d_2 = \frac{\zeta}{(\chi^2+\zeta^2)^{3/2}}. \tag{A4}$$

This system of linear equations can be solved using Cramer's method as

$$\chi'' = \frac{\Delta\chi''}{\Delta}, \qquad F' = \frac{\Delta F'}{\Delta}, \tag{A5}$$

where

$$\Delta\chi'' = c_1 b_2 - c_2 b_1, \tag{A6}$$

$$\Delta F' = a_1 c_2 - a_2 c_1, \tag{A7}$$

and

$$\Delta = a_1 b_2 - a_2 b_1. \tag{A8}$$

In a critical point, the denominator is $\Delta = 0$. This implies that

$$b_2 = \frac{a_2}{a_1} b_1, \tag{A9}$$

which explicitly means that

$$F^2 b^2 = \chi^2 + \zeta^2. \tag{A10}$$

Using equation (A9), equations (A6) and (A7) can be written as

$$\Delta\chi'' = \frac{b_1}{a_1}(a_2 c_1 - a_1 c_2), \qquad \Delta F' = -(a_2 c_1 - a_1 c_2). \tag{A11}$$

Because $b = \chi - \zeta\chi' > 0$ and $\chi' > 0$, except on the disk surface, $b_1 > 0$. Thus, the condition on the denominators, $\Delta\chi'' = \Delta F' = 0$, for a critical point reduces to

$$\zeta c_1 - \chi c_2 = 0, \tag{A12}$$

where equation (A10) was used to write $a_1 = \chi^2/b$. This condition can be written as

$$(\alpha - 1)(\zeta + \chi\chi') + \frac{\zeta b}{\chi}\left(1 + \frac{\epsilon_0}{\chi^2}\right) = 0. \tag{A13}$$

Since we consider $\alpha > 1$, all the terms are positive and the critical point can only be located at the disk surface where $\zeta = 0$, if $\chi' = 0$.

At the disk surface, the condition for a critical point, equation (A10) implies that

$$F(\epsilon_0,\ 0) = 1, \tag{A14}$$

i.e., the $\hat{z}$ velocity at the disk surface is the sonic speed (see eq. [10]). Applying L'Hopital's rule and assuming $F'(\epsilon_0,\ 0) \neq 0$, one obtains

$$F'(\epsilon_0,\ 0)^2 = \frac{-(\alpha^2 + \epsilon_0)}{2}, \tag{A15}$$

i.e., the velocity derivative at the disk surface has an imaginary value. Therefore, the mass injection at the disk surface cannot be sonic (the ionization front cannot be D type) and no critical points are allowed in the parametric equations.

REFERENCES

Akabane, K., Matsuo, H., Kuno, N., & Sugitani, K. 2001, PASJ, 53, 821

Akabane, A., Tsunekawa, S., Inoue, M., Kawabe, R., Ohashi, N., Kameya, O., Ishiguro, M., & Sofue, Y. 1992, PASJ, 44, 421

Allen, D. A. 1973, MNRAS, 161, 145

Altenhoff, W. J., Braes, L. L. E., Olnon, F. M., & Wendker, H. J. 1976, A&A, 46, 11

Altenhoff, W. J., Strittmatter, P. A., & Wendker, H. J. 1981, A&A, 93, 48

Altenhoff, W. J., Thum, C., & Wendker, H. J. 1994, A&A, 281, 161

Altenhoff, W. J., & Wendker, H. J. 1973, Nature, 241, 37

Baldwin, J. E., Harris, C. S., & Ryle, M. 1973, Nature, 241, 38

Beichman, C. A., Neugebauer, G., Habing, H. J., Clegg, P. E., & Chester, T. J. 1988, Infrared Astronomical Satellite (IRAS) Catalogs and Atlases, Vol. 1: Explanatory Supplement (NASA RP-1190; Washington, DC: NASA)

Blandford, R. D., & Payne, D. G. 1982, MNRAS, 199, 883

Blitz, L., Fich, M., & Stark, A. A. 1982, ApJS, 49, 183
Bloomer, J. D., et al. 1998, ApJ, 506, 727
Braes, L. L. E., Habing, H. J., & Shoenmaker, A. A. 1972, Nature, 240, 230
Campbell, B. 1984, ApJ, 282, L27
Campbell, B., & Thompson, R. I. 1984, ApJ, 279, 650
Cardelli, J. A., Clayton, G. C., & Mathis, J. S. 1989, ApJ, 345, 245
Chini, R., & Krugel, E. 1986, A&A, 167, 315
Clarke, C. J., Gendrin, A., & Sotomayor, M. 2001, MNRAS, 328, 485
Cohen, M., Bieging, J. H., Dreher, J. W., & Welch, W. J. 1985, ApJ, 292, 249
Danchi, W. C., Tuthill, P. G., & Monnier, J. D. 2001, ApJ, 562, 440
Dickel, H. R., Rots, A. H., Goss, W. M., & Forster, J. R. 1982, MNRAS, 198, 265
Downes, D., & Wilson, T. L. 1974, ApJ, 191, L77
Dreher, J. W., & Welch, W. J. 1983, AJ, 88, 1014
Escalante, V., Rodríguez, L. F., Moran, J. M., & Cantó, J. 1989, Rev. Mex. AA, 17, 11
Font, A. S., McCarthy, I. G., Johnstone, D., & Ballantyne, D. R. 2004, ApJ, 607, 890
Forster, J. R., Graham, D., Goss, W. M., & Booth, R. S. 1982, MNRAS, 201, 7P
Franco-Hernández, R., & Rodríguez, L. F. 2004, ApJ, 604, L105
Garcia-Arredondo, F., Arthur, S. J., & Henney, W. J. 2002, Rev. Mex. AA, 38, 51
Gaume, R. A., Goss, W. M., Wilson, T. L., & Johnston, K. J. 1995, ApJ, 438, 776
Gordon, M. A. 1992, ApJ, 387, 701
———. 2003, ApJ, 589, 953
Greenstein, J. L. 1973, ApJ, 184, L23
Gregory, P. C., & Seaquist, E. R. 1973, Nature Phys. Sci., 242, 101
Hackwell, J. A., Grasdalen, G. L., & Gehrz, R. D. 1982, ApJ, 252, 250
Hamann, F., & Simon, M. 1986, ApJ, 311, 909
Harris, S., & Scott, P. F. 1976, MNRAS, 175, 371
Hartmann, L., Jaffe, D., & Huchra, J. P. 1980, ApJ, 239, 905
Harvey, P. M., Thronson, H. A., Jr., & Gatley, I. 1979, ApJ, 231, 115
Henkel, C., Wilson, T. L., & Johnston, K. J. 1984, ApJ, 282, L93
Henney, W. J., Raga, A. C., Lizano, S., & Curiel, S. 1996, ApJ, 465, 216
Hjellming, R. M., Blankenship, L. C., & Balick, B. 1973, Nature Phys. Sci., 242, 84
Hollenbach, D., Johnstone, D., Lizano, S., & Shu, F. H. 1994, ApJ, 428, 654 (H94)
Hughes, V. A., & Woodsworth, A. 1973, Nature Phys. Sci., 242, 116
Hummer, D. G. 1988, ApJ, 327, 477
Israel, F. P. 1977, A&A, 59, 27
Johnstone, D., Hollenbach, D., & Bally, J. 1998, ApJ, 499, 758
Kameya, O., Morita, K., Kawabe, R., & Ishiguro, M. 1990, ApJ, 355, 562
Lee, T. A. 1970, PASP, 82, 765
Leinert, C. 1986, A&A, 155, L6
Madden, S. C., Irvine, W. M., Matthews, H. E., Brown, R. D., & Godfrey, P. D. 1986, ApJ, 300, L79
Martin, A. H. M. 1973, MNRAS, 163, 141
Martín-Pintado, J., Bachiller, R., Thum, C., & Walmsley, M. 1989, A&A, 215, L13
Martín-Pintado, J., Gaume, R., Bachiller, R., Johnston, K., & Planesas, P. 1993, ApJ, 418, L79
Martín-Pintado, J., Neri, R., Thum, C., Planesas, P., & Bachiller, R. 1994, A&A, 286, 890
Matsuyama, I., Johnstone, D., & Hartmann, L. 2003, ApJ, 582, 893
Menten, K. M., Reid, M. J., Moran, J. M., Wilson, T. L., Johnston, K. J., & Batrla, W. 1988, ApJ, 333, L83
Minier, V., Booth, R. S., & Conway, J. E. 1998, A&A, 336, L5
———. 2000, A&A, 362, 1093
Momose, M., Tamura, M., Kameya, O., Greaves, J. S., Chrysostomou, A., Hough, J. H., & Morino, J. I. 2001, ApJ, 555, 855
Nesterov, N. S. 1990, Izv. Krymskoi Astrofiz. Obs., 82, 45
Norris, R. P., Booth, R. S., Diamond, P. J., & Porter, N. D. 1982, MNRAS, 201, 191
Odenwald, S., Shivanandan, K., & Thronson, H. A., Jr. 1992, PASP, 104, 127
Panagia, N., & Felli, M. 1975, A&A, 39, 1
Perrenod, S. C., & Lada, C. J. 1979, ApJ, 234, L173
Pestalozzi, M. R., Elitzur, M., Conway, J. E., & Booth, R. S. 2004, ApJ, 603, L113
Planesas, P., Martín-Pintado, J., & Serabyn, E. 1992, ApJ, 386, L23
Pratap, P. 1990, Ph.D. thesis, Univ. Illinois
Pratap, P., Batrla, W., & Snyder, L. E. 1989, ApJ, 341, 832
Pratap, P., Snyder, L. E., & Batrla, W. 1992, ApJ, 387, 241
Purton, C. R., Feldmann, P. A., & Marsh, K. A. 1982, MNRAS, 198, 321
Richling, S., & Yorke, H. W. 1997, A&A, 327, 317
Rodríguez, L. F., & Bastian, T. S. 1994, ApJ, 428, 324
Rots, A. H., Dickel, H. R., Forster, J. R., & Goss, W. M. 1981, ApJ, 245, L15
Schaller, G., Schaerer, D., Meynet, G., & Maeder, A. 1992, A&AS, 96, 269
Schwartz, P. R. 1980, PASP, 92, 534
Schwartz, P. R., & Spencer, J. H. 1977, MNRAS, 180, 297
Scoville, N. Z., Sargent, A. I., Sanders, D. B., Claussen, M. J., Masson, C. R., Lo, K. Y., & Phillips, T. G. 1986, ApJ, 303, 416
Shu, F. H., Johnstone, D., & Hollenbach, D. 1993, Icarus, 106, 92
Shu, F. H., Lizano, S., Galli, D., Cantó, J., & Laughlin, G. 2002, ApJ, 580, 969
Simon, T., & Dyck, H. M. 1977, AJ, 82, 725
Steppe, H., Salter, C. J., Chini, R., Kreysa, E., Brunswig, W., & Lobato Perez, J. 1988, A&AS, 75, 317
Steppe, H., et al. 1993, A&AS, 102, 611
Störzer, H., & Hollenbach, D. 1999, ApJ, 515, 669
Strelnitski, V., Haas, M. R., Smith, H. A., Erickson, E. F., Colgan, S. W. J., & Hollenbach, D. J. 1996, Science, 272, 1459
Tafoya, D., Gómez, Y., & Rodríguez, L. F., 2004, ApJ, 610, 827
Thronson, H. A., Jr., & Harper, D. A. 1979, ApJ, 230, 133
Thum, C., Martín-Pintado, J., & Bachiller, R. 1992, A&A, 256, 507
Turner, B. E., & Matthews, H. E. 1984, ApJ, 277, 164
Ulich, B. L. 1981, AJ, 86, 1619
Vergely, J.-L., Egret, D., Freire Ferrero, R., Valette, B., & Koeppen, J. 1997, in Proc. ESA Symp. "Hipparcos—Venice '97" (ESA SP-402; Noordwijk: ESA), 603
Wendker, H. J., Higgs, L. A., & Landecker, T. L. 1991, A&A, 241, 551
Werner, M. W., Becklin, E. E., Gatley, I., Matthews, K., Neugebauer, G., & Wynn-Williams, C. G. 1979, MNRAS, 188, 463
White, R. L., & Becker, R. H. 1985, ApJ, 297, 677
Wink, J. E., Altenhoff, W. J., & Mezger, P. G. 1982, A&A, 108, 227
Wink, J. E., Altenhoff, W. J., & Webster, W. J., Jr. 1975, A&A, 38, 109
Wood, D. O. S. W., & Churchwell, E. 1989, ApJS, 69, 831
Woodsworth, A. W., & Hughes, V. A. 1977, A&A, 58, 105
Woody, D. P., Scott, S. L., Scoville, N. Z., Mundy, L. G., Sargent, A. I., Padin, S., Tinney, C. G., & Wilson, C. D. 1989, ApJ, 337, L41
Wynn-Williams, C. G., Becklin, E. E., & Neugebauer, G. 1974, ApJ, 187, 473
Yorke, H. W., & Welz, A. 1996, A&A, 315, 555
Zoonematkermani, S., Helfand, D. J., Becker, R. H., White, R. L., & Perley, R. A. 1990, ApJS, 74, 181